Article

Visualizing MRI Deep Learning Segmentation Algorithms using 3D Printing

Greg Tyler [1], Oliver Mathias [2, *] and Andrew Papilion [2]

Chapman University, Orange CA, USA
1 gtyler@chapman.edu
2 mathias@chapman.edu
3papilion@chapman.edu
* Correspondance: mathias@chapman.edu

Abstract: As the capabilities and roles of Artificial Intelligence (AI) in the medical field are continually expanded, new potential uses, and combinations of technology become viable. This paper highlights a methodology for utilizing AI Magnetic Resonance Imaging (MRI) segmentation networks and 3D printing processes in conjunction for medical diagnosis, planning, and visualization of medical images. We also include promising benefits and potential medical offerings made possible by this system. By training a "U- Net" on the 2019 BraTS dataset, we base our research on an MRI brain lesion segmentation dataset with sustaining performance and world recognition. This network automatically segments novel MRI scans into lesion and non-lesion regions. We pair this network with a 3D printing process that enables us to print fully segmented, 1:1 scale, patient organs aided by AI techniques to better explain cases, test models, and plan for operations. In addition to a clearly outlined process that enables these offerings, we establish a potential trajectory for how these combined tools will continue to revolutionize the ways healthcare professionals interact with patients and their data.

Keywords: AI Segmentation, 3D Printing, MRI, MRI Visualization

1. Introduction

Stereolithography, more colloquially known as "3D Printing", has been around for over 40 years [1]. In that time, the technology has transformed from an expensive prototyping technique predominantly used by engineers, to a tool used by surgeons, rocket scientists, auto manufacturers, and hobbyists alike.12 3D printing differs tremendously from other manufacturing techniques due to its inherent "additive manufacturing" characteristic or "layer by layer" material stacking. In normal manufacturing processes, materials such as plastic or aluminum are heated to their melting points and shaped by large, complex, machinery. This approach provides high output volumes for a single product but it is often expensive to modify and repair. Alternatively for 3D printing, the entire manufacturing process contained within the 3D printer, allowing for easier modifications, repairs, and rapid changes in producing an end-product. 3D printing using "additive" functionality stems from the process of extruding heated material layer by layer to create a final shape, with each layer of material building on the previously cooled layer.

The instructions needed for accurate layers and amounts of filament are created by importing a 3D file, most commonly a Stereolithography file or .STL, into a program called a "slicer". A slicer takes an .STL file and converts it to instructions that the printer programs to direct its mechanical components, the filament extruder, stepper motors, and heated tip to execute in order to build the 3D model.

The output of these slicers is a G-Code file that contains all relevant information needed for the printer to create each layer of the 3D model. This G-Code file can then be loaded into the printer to carry out the printing process. "G-Code" file instructions will vary from the original model to ensure structural integrity during printing. STL files only contain information defining the outermost layer's dimensions leading to essentially hollow 3D computer models. To combat negative printing effects associated with hollow 3D models, namely the warping of the model from lack of support material, slicers add what is referred to as "in-fill." In-fill is simply a repeating geometric pattern infused into the hollow parts of a 3D model. Shown below in Figure 1 are varying densities of infill, which can range from 0% to 100%, and adds structural integrity to the model to prevent ill-effects like warping.
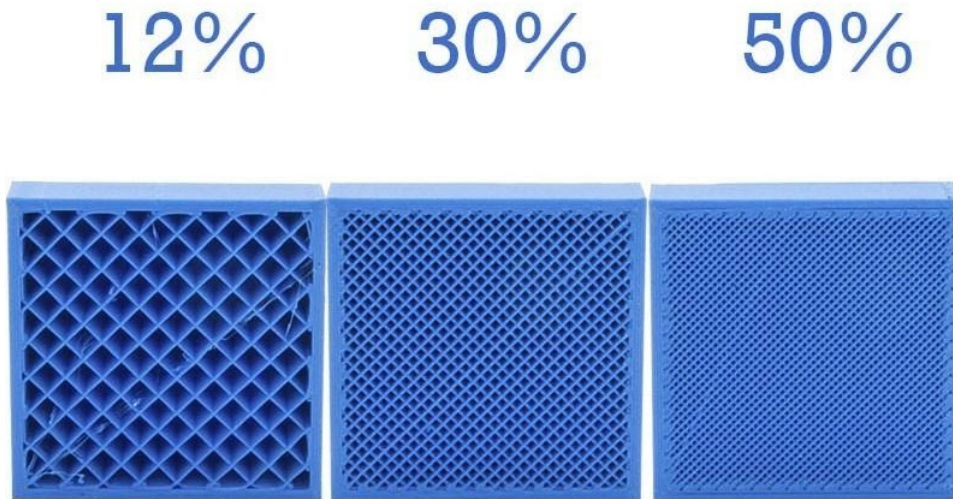
Figure 1. In-fill with different intensity.

If a 3D model's external design includes angles and overhangs that cannot be printed without deforming the original model due to gravity, extra external material may be required to "support" the original model. These "supports" are also calculated and added to the "G-Code" in the slicer program. Examples of the use of supports in 3D printing is shown in Figure. 2.
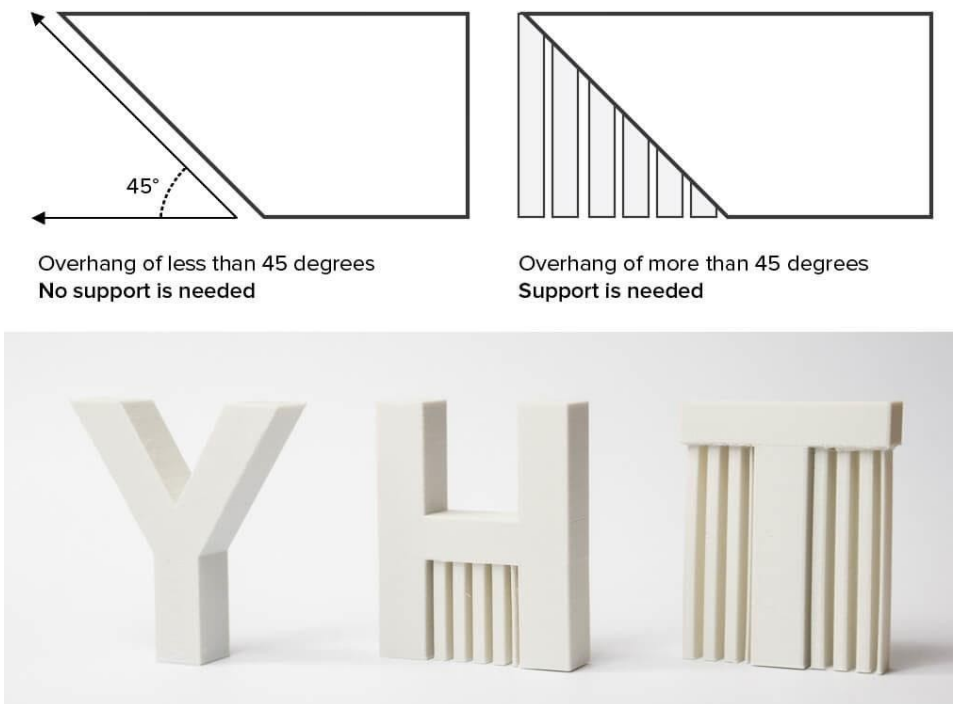

Figure. 2. Examples of the use of supports in 3D printing.

The only inputs for the printer are a "G-Code" file, containing the layer by layer instructions for printing, and a spool of filament that can range in material composition from plastic and wood, to metal and carbon fiber [2]. Advancements in 3D printing hardware such as Prusa3D's Multi Material Upgrade 3 allow users to print in 5 materials at once, providing increasingly complex models and manufacturing techniques to soon be available to consumers [3].

This rapid advancement in material types and multi-material printing hardware has huge implications for prototyping and cost reduction in the field of medicine. Two popular 3D printing applications to volumetric medical data include patient education and surgical planning. Studies have illustrated that patients, given the ability to interactively see their anatomy through 3D models of Computed Tomography (CT) or MRI scans, exhibit an increased understanding of the procedure 4 and improved satisfaction with

the quality of care [4,5]. For the individual medical professional, specifically a surgeon, 3D prints can be used for preoperative planning, as well as helping customize implants to the patient's bone structure [6]. Successes in maxillofacial procedures have shown a 23% reduction in operation times when 3D models were used to shape titanium plates to a patient's bone structure before the operation [7].

1.1 Overview on AI MRI Segmentation in Medicine

"Artificial Intelligence" (AI), or in this case Convolutional Neural Network (CNN) is an umbrella term for algorithms whose architectures mimic that of neurons interacting within the human brain. These algorithms find patterns based on large amounts of data; which can come in the form of labeled or unlabeled images, sound, text, matrices of values, etc. This technology has huge implications for the cost, profitability, and reach of hospitals and medical providers around the world.

Among the fastest developing and maturing uses of AI in medicine surrounds the field of dermatology. With some of the most easily collectible data for training, researchers around the world have begun their search for clinical grade AI applications in the problem of diagnosing 'malignant" and "benign" skin lesions. In 2017 Stanford University, with a training set of 129,450 clinical images that included 2,032 skin diseases, trained a "Convolutional Neural Network", which is an image processing centered AI algorithm, to diagnose these diseases on a level similar to 21 board certified Dermatologists [8]. The output of these models is a vector containing "confidence variables" associated with each lesion type encompassed in the training data. In the same year, at the International Skin Imaging Collaboration (ISIC), the winner's AI algorithm was able to distinguish between melanomas and benign moles with 98% accuracy [9]. These undercurrents of easily accessible data as well as initially promising results from scientific studies have spurred the creation of mobile applications such as DermEngine, SkinVision, and SkinIO which have promised a shift towards a universally accessible and affordable skin lesion diagnosis system [10].

In the field of radiology, similar steps are being undertaken to introduce AI into patient diagnoses. While Radiology stands to gain just as much as the Dermatological industry from these advancements, the difference in data necessary for training makes progress more difficult. The training data associated with classifying Dermatological lesions, namely color images with an associated lesion classification by a Dermatologist, is more accessible, both in compatibility and ease of creation than the training data associated with radiology [11].

In the Radiological industry, more specifically when dealing with MRI technology surrounding soft tissue diagnoses, output data is more complex and carries with it the risk of patient identification, and thus more effort is required to transfer, access, and segment said data. MRI scans are packaged in "DICOM" or "Nifti" format, these files contain a small metadata header portion and a number of "slices" that make up the scan. These slices are 2D matrices that contain values associated to the amount of water at each pixel in the scan [12].These 2D matrices can be stacked to build a 3D visualization of the full scan.

Because these files are made up of 2D matrices, they can be treated as grayscale images and therefore can have "U-Nets" applied to them. These networks, given their name from the fact that their architecture is popularly drawn in the symmetrical "U" shape, analyze images via a similar internal process as the "CNNs", however, they differ in the process of creating training data and in the resulting model's output. While dermatology training data pairs include an image and a disease label, taking the place of a dermatologist's diagnosis, an MRI scan is commonly labeled pixel by pixel. This "pixel by pixel" labeling is known as "segmentation" and can be seen in Figure 3 below. Unlike the opaque confidence values of Dermatological AI, segmenting offers pixel by pixel attribution to specific tissues, healthy, cancerous, etc. As one can imagine this offers much greater insight into the progress of diseases, but carries with it a much higher cost of acquisition, as trained professionals must not only diagnose each scan, but segment its tissues into distinct groups.

The figure below shows the same type of segmented images as described above. More specifically, it provides an intuitive comparison between "true" segmented images and the "predicted" segmented outputs of an Nvidia developed and trained "U-Net like network" [13].
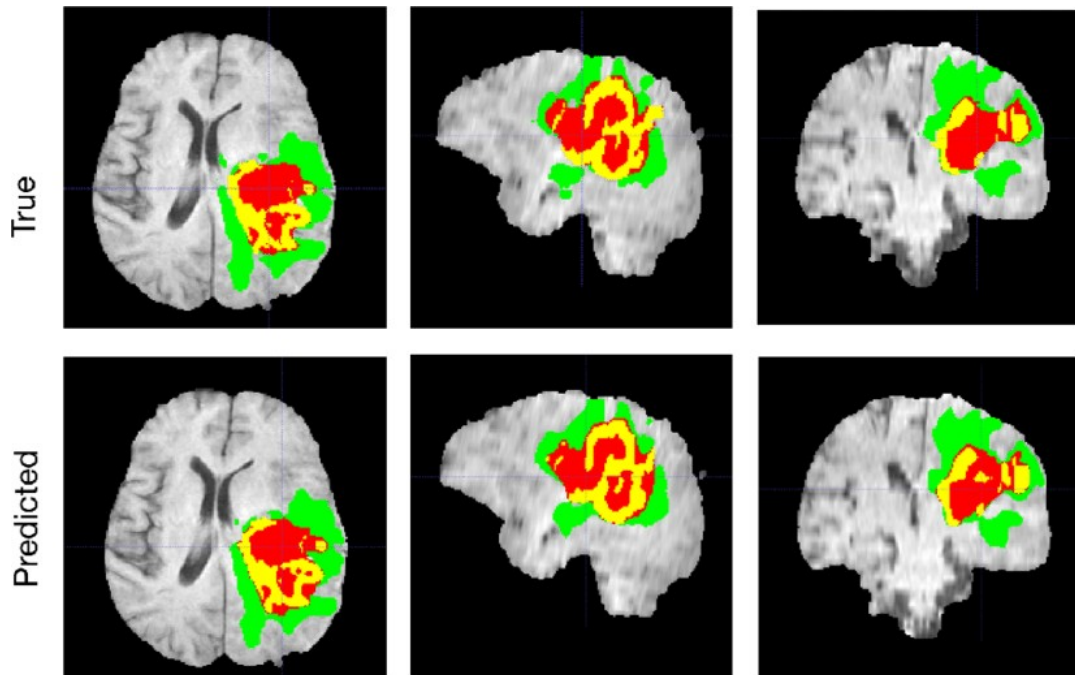
Figure 3. A typical segmentation example with true and predicted labels overlaid over T1c MRI axial, sagittal and coronal slices (r to l). The whole tumor (WT) class includes all visible labels (a union of green, yellow and red labels), the tumor core (TC) class is a union of red and yellow, and the enhancing tumor core (ET) class is shown in yellow (a hyperactive tumor part). The predicted segmentation results match the ground truth well. Courtesy of Ref. [13]

1.2 Combining the AI predictive analytics with the visualizations of 3D printing

The genesis of this project is in the recognition of similarities in AI segmented MRI data and data input to the 3D printing process. The "layer by layer" representations of human anatomy in MRI files matched the structure of the data being fed into 3D printers almost perfectly, leading to a natural representation of these segmented scans in 1:1 scale if consumer grade 3D printers are employed.

After conducting a search on the current state of the art of AI MRI segmentation tools that display both high segmentation accuracy and are developed using tools that allow for easy modification of said networks and pipelines, we settled on modifying the 3D U-Net architecture developed by Özgün Çiçek and A. Abdulkadir at the University of Freiburg, Germany which we found, among other alternatives, to display high segmentation accuracy with tools easy for modification of said networks and pipelines [14]. We chose it as our base for analytics and visualization in combining AI and 3D printing techniques. An added benefit of the 3D U-Net is that an example usage has been open sourced by MATLAB which includes a pre-trained network on the 2017 BraTS dataset [15]. Thanks to its superior ability to easily manipulate matrices, and in our case, make data and pipeline modifications quickly, building in the MATLAB example further proved to be a prudent decision.

Figure 4 below highlights the architecture of the 3D U-Net sourced from MATLAB's "3-D Brain Tumor Segmentation Using Deep Learning" [15]. Starting with an input matrix of shape (132,132,132,4), this matrix, representing the x, y, and z axes respectively, with a fourth dimension for image modality, is then passed through two convolution, batch norm, and Rectified Linear Unit (ReLU) layers. The convolution layers have a kernel size of (2x2x2) and the batch norm layers have a kernel size of (1x1x1). The output feature map from this "processing block" has the shape (128,128,128,64). It is then passed through a max pooling layer with a kernel size of 2x2x2, resulting in a feature map shape of (64,64,64,64). These "processing blocks" are repeated until reaching a feature map shape of (9,9,9,512). when it concludes the processes on the "left-side" of the U-Net.

All remaining "processing blocks" on the "right-side" of the U-Net "up convolute" the feature maps, i.e., making them larger. Each "processing block" is made up of an "Up Convolution" with kernel size (2x2x2), a "Crop and Concatenate" portion, and like the "left side" processing blocks, two convolution, batch norm, and ReLU groups. Starting from the previous (9,9,9,512) feature map, the first "right-side" processing block "up convolutes" the feature map to shape (18,18,18,512) and concatenates a cropped feature map of shape (18,18,18,256) from the second to last "left-side processing block." After this feature map of size (18,18,18,768) is created, it is passed through the two convolution, batch norm, and ReLU layer groups, resulting in a feature map shape of (14,14,14,256). These "Up Convolution" processing blocks are continued until a feature map shape of (44,44,44,64) is reached. The

next layers, a convolution layer with a (21,1,1) kernel size, and a SoftMax layer, lead to an output matrix of shape (44,44,44,2). This output segmentation map with x, y, and depth measurements of 44 pixels, also includes a fourth dimension for the two classifications: cancerous tissue and non-cancerous tissue.
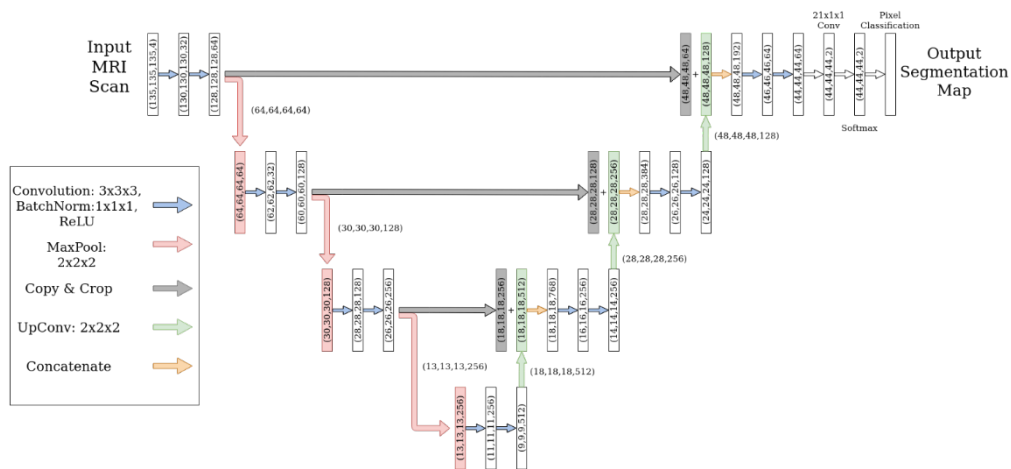

Figure 4. U-Net Architectural Diagram

[Note that the output matrix is smaller than the input matrix thanks to the non-padded layers within the network. However, the original creators of this network have noted that: "With a voxel size of $1.76 \times 1.76 \times 2.04 \ \mu m^3$, the approximate receptive field becomes $155 \times 155 \times 180 \ \mu m^3$ for each voxel in the predicted segmentation. Thus, each output voxel has access to enough context to learn efficiently."]

2. Materials and Methods

As stated in the section above, our dataset and model selection was based on the ease of modification of the code, and to a lesser extent, the computing power and time necessary to train our network. As the estimated training time for the U-Net MATLAB model on the BraTS 2017 dataset is around 30 hours on a machine with 4 Titan X GPUs, it is prudent to start with a pre-trained model.

Characteristics of data pre-processing steps, and model training parameters engaged in MATLAB, are summarized below [15].

The 2017 BraTS dataset contains 750 MRI scan matrices, of which are the shape (240, 240, 155, 4). Of the 750 scans, 484 are labeled and 266 are un-labeled test scans. The 484 labeled scans were split into training, validation, and test sets for the training of this network; with the final count being 400 in the training set, 29 in the validation set, and 55 in the test set. Each modality in each volume was then normalized by "subtracting the mean and dividing by the standard deviation of the cropped brain region 15."

Patch sizes of 132 x 132 x 132 voxels for the training data and its corresponding pixel label data, as well as the validation and test data were chosen. Finally, the "augmentAndCrop3dPatch" function was implemented which randomly rotated and reflected the training data, and cropped "response patches" to the output size of the network 44 x 44 x 44 voxels [15]. The most pertinent training parameters used are listed in Table 1 below.

Table 1. Training Parameters for MATLAB Modeling

Optimizer	Adam	Common Industry Values
Initial Learning Rate	0.00005	.00001 - .0001
Learn Rate Dropout Period	5	10
Learn Rate Dropout Factor	0.95	0.75 - 1
Mini-Batch Size	8	4 - 32

The pre-trained MATLAB model has an average dice score of the "background" label of the segmentation map across five test volumes of 0.9993 with an average dice score of the "tumor" label of the segmentation map across five test volumes of 0.9585. Given that this is a small dataset, overfitting is a concern, however, the results are of high enough quality to proceed with our 3D printing procedures.

The first step in our pipeline is to convert the output matrix into a ".nii" file, which stands for "NIfTI-1 Data Format" and is a popular neuro-imaging file type, similar to DICOM. This new ".nii" file contains the same information as the output matrix of the model, "background" or non-cancerous voxels, and "tumor" voxels. Now with a file format compatible with most neuro-imaging software we opened the file in "3D Slicer" a popular MRI viewing application, where the data can be inspected for accuracy/deformations and output into the STL or "Stereolithography" format required by 3D printers.

Before the output occurs, we must perform "thresholding" on the data in 3D Slicer. This process allows us to select all voxels within a certain color range. After visually confirming that all "background" and "tumor" voxels had been separately selected, the output was generated in two distinct STL files.

These two STL files were then opened in a popular, open source, 3D model editing application, Slic3r. These STL models were placed in the correct position once more and they were split down the Sagittal plane for improved viewing of the tumor versus healthy tissues.

One hemisphere was chosen, containing both healthy and AI labeled cancerous tissue to be imported into "Prusa Slicer", which is the native software accompanying our Prusa MK3S with the additional MMU3s multi material print head [16].

Inside "Prusa Slicer," each STL that makes up the selected hemisphere was assigned a "print head" along with a filament type and color. We chose Red "Prusament" PLA filament to represent the healthy tissue, and Gray "Prusament" PLA filament to represent the cancerous tissue. This full process is shown in Figure 5.
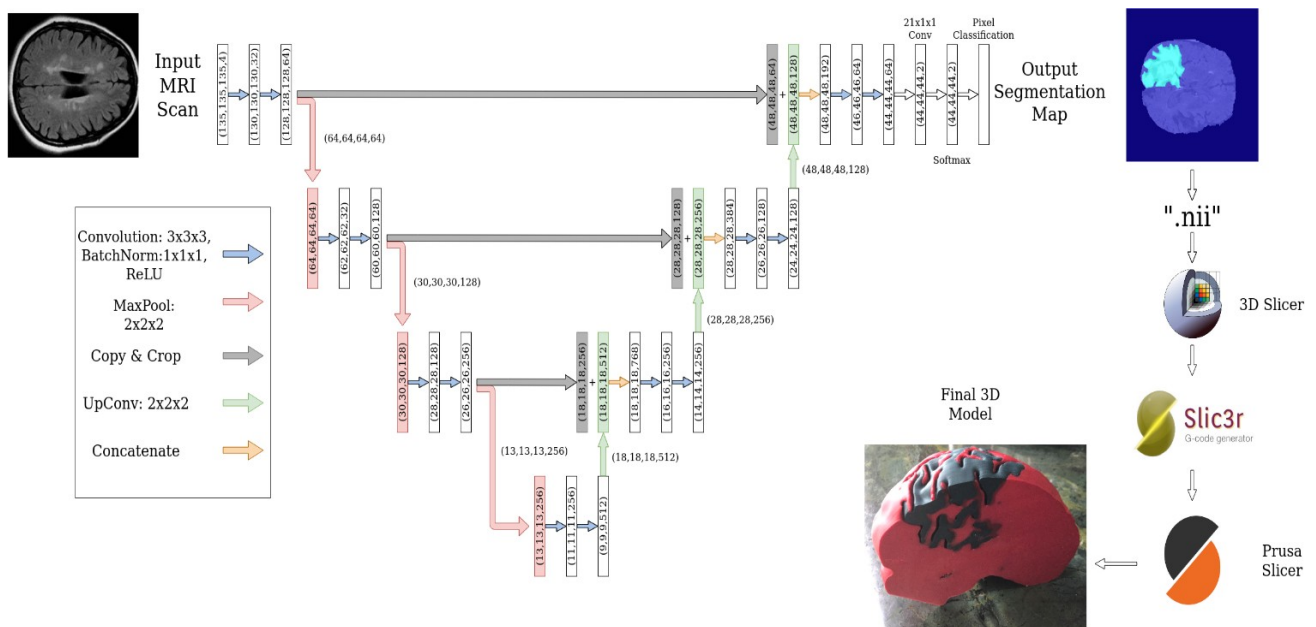

Figure 5. Process combining AI Segmentation and 3D Printing

3. Results

To generate a 1:1 model for research purposes, 375.87 g of filament was used, the printing time was 1 d 4 h 57 min, requiring 324 print head changes, at a total cost of $9.55. The materials used for this print are red and gray Prusa brand PLA filament in a Prusa MK3S and Prusa MMU3S printer.

1. the ease of printing,
2. low cost,
3. requiring small amount of manual labor, and
4. anatomical accuracy of the model.

By utilizing available technology, not only do we provide a method for serving the medical community with a low-cost tool for analyzing MRI data of cancerous brain tumors, we also aim to entice the possibilities that arise from printing other anatomical structures. The output of our process is shown in Figure 6.

Figure 6. A top level view of a finished print.

The final product of the printing process yields an anatomically accurate 1:1 ratio 3D printed model, allowing the internal structure of the tumor to be visualized in grey colored filament. By using multi-colored models, key differences are highlighted in the healthy brain tissue versus the cancerous brain tissue. These results enable a unique approach to analyzing medical data, where not only is patient data able to be visualized, but in a manner that allows hands-on interaction with internal biological structures. This research focuses on bringing to life cancerous brain tumors in an intuitive manner. The technique can be easily transferable to any other internal structure of the body.

4. Conclusions

By combining AI segmented MRI data with consumer 3D printing technology and techniques, we have showcased a robust method for producing anatomically accurate 3D models that can serve as a new avenue for examining patient data, providing better aid for medical diagnoses and a unique tool for pre-operative planning. Through comparing human segmented MRI data with AI segmented data, our results echoed the accuracy that can be achieved through training a neural network to perform MRI segmentation, and how leveraging these results with readily available 3D printing technology enables an unprecedented approach to examining patient data, all at financially viable cost for any medical research institution. With exciting advancements in AI and 3D printing, the future of medicine holds remarkable potential for these combined technologies to offer a novel partnership and enable further breakthroughs..

References

1. History of 3D Printing Timeline: Who Invented 3D Printing. 3D Insider. 2018; published online Feb https://3dinsider.com/3d- printing-history/ (accessed Dec 6, 2020)
2. 16 Types of 3D Printer Filaments. 3D Insider. 2019; published online April 4. https://3dinsider.com/3d-printing-materials/ (accessed Dec 6, 2020).
3. Original Prusa i3 Multi Material 2.0 - Prusa3D - 3D Printers from Josef Průša. Prusa3D. 2018; published online Aug 30. https://www.prusa3d.com/original-prusa-i3-multi-material-2-0/ (accessed Dec 6, 2020).

4. Biglino G., Capelli C., Wray J., et al. 3D-manufactured patient-specific models of congenital heart defects for communication in clinical practice: feasibility and acceptability. *BMJ Open* **2015**, 5. DOI:10.1136/bmjopen-2014-007165.

5. Zhuang Y-D., Zhou M-C., Liu S-C., Wu J-F., Wang, R., Chen, C-M. Effectiveness of personalized 3D printed models for patient education in degenerative lumbar disease. *Patient Education and Counseling* **2019**, *102*: 1875–81.

6. Ghai S., Sharma Y., Jain N., Satpathy M., Pillai AK. Use of 3-D printing technologies in craniomaxillofacial surgery: a review. *Oral and Maxillofacial Surgery* **2018**, *22*: 249–59.

7. Gil RS, Roig AM, Obispo CA, Morla A, Pagès CM, Perez JL. Surgical planning and microvascular reconstruction of the mandible with a fibular flap using computer-aided design, rapid prototype modelling, and precontoured titanium reconstruction plates: a prospective study. *British Journal of Oral and Maxillofacial Surgery* **2015**, *53*: 49–53.

8. Esteva A, Kuprel B, Novoa RA., et al. Dermatologist-level classification of skin cancer with deep neural networks. *Nature* **2017**; *542*: 115–8.

9. Codella NCF, Gutman D, Celebi ME, et al. Skin Lesion Analysis Toward Melanoma Detection: A Challenge at the 2017 International Symposium on Biomedical Imaging (ISBI), Hosted by the International Skin Imaging Collaboration (ISIC). arXiv.org. 2018; published online Jan 8. https://arxiv.org/abs/1710.05006 (accessed Dec 7, 2020).

10. Utermohlen K. 4 Applications of Artificial Intelligence (AI) on Dermatology. Medium. 2018; published online May 22. https://medium.com/@karl.utermohlen/4-applications-of-artificial-intelligence-ai-on-dermatology-33991c97f05b (accessed Dec 7, 2020).

11. Du-Harpur X, Watt FM, Luscombe NM, Lynch MD. What is AI? Applications of artificial intelligence to dermatology. Wiley Online Library. 2020; published online March 29. https://onlinelibrary.wiley.com/doi/full/10.1111/bjd.18880 (accessed Dec 7, 2020).

12. Nora Maria Raschle, Udochukwu Amanamba, Gabrielle-Ann A. Torre, Melissa Eaton. The Physics of MRI and How We Use It to Reveal the Mysteries of the Mind. Frontiers for Young Minds. https://kids.frontiersin.org/article/10.3389/ frym.2019.00023 (accessed Dec 7, 2020).

13. Myronenko A, Hatamizadeh A. Robust Semantic Segmentation of Brain Tumor Regions from 3D MRIs. arXiv.org. 2020; published online Jan 6. https://arxiv.org/abs/2001.02040 (accessed Dec 7, 2020).

14. Çiçek Ö, Abdulkadir A, Lienkamp SS, Brox T, Ronneberger O. 3D U-Net: Learning Dense Volumetric Segmentation from Sparse Annotation. Medical Image Computing and Computer-Assisted Intervention – MICCAI 2016 Lecture Notes in Computer Science 2016; : 424–32.

15. 3-D Brain Tumor Segmentation Using Deep Learning. MATLAB & Simulink Example. https://www.mathworks.com/help/deeplearning/ug/segment-3d-brain-tumor-using-deep-learning.html (accessed Dec 7, 2020).

16. PrusaSlicer - Prusa3d.com - 3D printers by Josef Prusa. Prusa3D. 2019; published online May 16. https://www.prusa3d.com/ prusaslicer/ (accessed Dec 7, 2020).

17. Patel VL, Shortliffe EH, Stefanelli M, et al. The coming of age of artificial intelligence in medicine. *Artificial Intelligence in Medicine* **2009**, *46*: 5–17.

18. Krittanawong C. The rise of artificial intelligence and the uncertain future for physicians. *European Journal of Internal Medicine* **2018**, *48*. DOI:10.1016/j.ejim.2017.06.017.

19. Ahuja AS. The impact of artificial intelligence in medicine on the future role of the physician. PeerJ 2019; 7. DOI:10.7717/ peerj.7702.

20. Liew C. The future of radiology augmented with Artificial Intelligence: A strategy for success. *European Journal of Radiology* **2018**, *102*: 152–6.

21. Lau I, Sun Z. Three-dimensional printing in congenital heart disease: A systematic review. *Journal of Medical Radiation Sciences* **2018**, *65*: 226–36.

22. Loke Y-H, Harahsheh AS, Krieger A, Olivieri LJ. Usage of 3D models of tetralogy of Fallot for medical education: impact on learning congenital heart disease. *BMC Medical Education* **2017**, 17. DOI:10.1186/s12909-017-0889-0.

23. Francoisse CA, Sescleifer AM, King WT, Lin AY. Three-dimensional printing in medicine: a systematic review of pediatric applications. *Pediatric Research* **2020**; published online June 5. DOI:10.1038/s41390-020-0991-6.

24. Richens JG, Lee CM, Johri S. Improving the accuracy of medical diagnosis with causal machine learning. *Nature Communications* **2020**; *11*. DOI:10.1038/s41467-020-17419-7.

25. Pacilè S, Lopez J, Chone P, Bertinotti T, Grouin JM, Fillard P. Improving Breast Cancer Detection Accuracy of Mammography with the Concurrent Use of an Artificial Intelligence Tool. Radiology: Artificial Intelligence 2020; 2. DOI:10.1148/ ryai.2020190208.

26. Wang DD, Qian Z, Vukicevic M, et al. 3D Printing, Computational Modeling, and Artificial Intelligence for Structural Heart Disease. JACC: Cardiovascular Imaging 2020; published online Aug 26. DOI:10.1016/j.jcmg.2019.12.022.

27. Farhat W, Chatelain F, Marret A, et al. Trends in 3D bioprinting for esophageal tissue repair and reconstruction. *Biomaterials* **2021**, *267*: 120465.

28. Mironov V, Reis N, Derby B. Review: Bioprinting: A Beginning. *Tissue Engineering* **2006**, *12*: 631–4.

29. Vijayavenkataraman S, Yan W-C, Lu WF, Wang C-H, Fuh JYH. 3D bioprinting of tissues and organs for regenerative medicine. *Advanced Drug Delivery Reviews* **2018**, *132*: 296–332.

30. Marzio ND, Eglin D, Serra T, Moroni L. Bio-Fabrication: Convergence of 3D Bioprinting and Nano-Biomaterials in Tissue Engineering and Regenerative Medicine. *Frontiers in Bioengineering and Biotechnology* **2020**, *8*. DOI:10.3389/ fbioe.2020.00326.

31. Moroni L, Boland T, Burdick JA, et al. Biofabrication: A Guide to Technology and Terminology. *Trends in Biotechnology* **2018**, *36*: 384–402.

32. Victorino JP, Wilson DM. Investigating moral distress over a shortage of organs for transplantation. *Revista Bioética* **2020**, *28*: 83–8.

33. Ng WL, Chan A, Ong YS, Chua CK. Deep learning for fabrication and maturation of 3D bioprinted tissues and organs. *Virtual and Physical Prototyping* **2020**, *15*: 340–58.

34. Xie Z, Gao M, Lobo AO, Webster TJ. 3D Bioprinting in Tissue Engineering for Medical Applications: The Classic and the Hybrid. *Polymers* **2020**, *12*: 1717.

35. Murphy SV, Atala A. 3D bioprinting of tissues and organs. *Nature Biotechnology* **2014**, *32*: 773–85.